

Fabrication of a (K,Na)NbO₃-based lead-free 1-3 piezocomposite for high-sensitivity ultrasonic transducers application

EP

Cite as: J. Appl. Phys. 125, 214501 (2019); doi: 10.1063/1.5088171

Submitted: 8 January 2019 · Accepted: 11 May 2019 ·

Published Online: 4 June 2019



View Online



Export Citation



CrossMark

Laiming Jiang,^{1,2,a),b)} Ruimin Chen,^{3,a)} Jie Xing,¹ Gengxi Lu,³ Runze Li,^{2,3} Yue Jiang,¹ K. Kirk Shung,³ Jianguo Zhu,^{1,b)} and Qifa Zhou^{2,3,b)}

AFFILIATIONS

¹College of Materials Science and Engineering, Sichuan University, Chengdu 610064, China

²Roski Eye Institute, Keck School of Medicine, University of Southern California, Los Angeles, California 90033, USA

³Department of Biomedical Engineering, Viterbi School of Engineering, University of Southern California, Los Angeles, California 90089, USA

a)Contributions: L. Jiang and R. Chen contributed equally to this work.

b)Authors to whom correspondence should be addressed: 15208287686@126.com, nic0400@scu.edu.cn, and qifazhou@usc.edu

ABSTRACT

Ultrasonic imaging is a well-established powerful medical diagnosis tool at present. However, commercial ultrasonic transducers are commonly made of toxic lead-based piezoelectric materials. Thus, it is vital to develop lead-free alternatives with satisfactory performance. This study presents the development of a phase boundary-engineered (K,Na)NbO₃-based lead-free 1-3 piezocomposite and its application on high-sensitivity ultrasonic imaging transducers. A modified dice-and-fill technique was used to manufacture the micro-scale piezocomposite, by which the ceramic pillars were miniaturized to a width of 55 μm with a kerf of 15 μm. Improved acoustic and electrical properties were obtained in the new piezocomposite, and ultrasonic imaging transducers were further designed and fabricated based on the composite. The fabricated transducers exhibit enhanced performance with a high center frequency (16 MHz), a broad bandwidth (83%), and a very low insertion loss (9.8 dB), outperforming state-of-the-art transducers based on other lead-free materials. Imaging capability of the transducers was evaluated via *ex vivo* imaging of a porcine eyeball, indicating that this lead-free piezocomposite has many attractive properties in developing environment-friendly high-sensitivity ultrasonic devices for biomedical imaging applications.

Published under license by AIP Publishing. <https://doi.org/10.1063/1.5088171>

I. INTRODUCTION

Attributable to its high efficiency, lack of ionizing radiation exposure, and noninvasive characteristics, ultrasonic imaging technology plays a vital role in current medical diagnostics.^{1–3} It has been extensively used in cardiology, obstetrics and gynecology, ophthalmology, etc.^{4,5} In ultrasonic imaging, the performance of the transducer plays a critical role in determining the image quality.⁶ Selection of the piezoelectric materials is the first decision to be made in developing high-performance ultrasonic transducers with high sensitivity and broad bandwidth. As the key active element inside the device, properties of the piezoelectric materials have a significant effect on the performance of the transducer.

At present, lead-based piezoelectric materials represented by lead zirconate titanate (PZT) and their related lead-based perovskites are dominant in the piezoelectric market on account of their outstanding piezoelectric properties.^{7,8} Nevertheless, there has been worry in recent years that these lead-based materials which contain toxic lead oxide are harmful to human health, especially in clinical medicine that typically requires direct and close contact with the human body.⁹ Moreover, there is a raised social awareness of environmental protection and released directive on Restriction of the Hazardous Substances (RoHS),¹⁰ making it vital to develop novel environmentally friendly lead-free medical devices as lead-based alternatives.

Over the past few decades, there have been numerous research studies on developing environment-friendly lead-free piezoelectric materials, mainly including BaTiO₃ (BT), (Bi_{1-x}Na_x)TiO₃ (BNT), BiFeO₃ (BFO), and (K_{1-x}Na_x)NbO₃ (KNN)-based piezoceramics.^{8,11–17} Nevertheless, their further developments are hindered by some shortcomings, such as low Curie temperature for BT-based series,¹⁷ inferior piezoelectric performance for BNT-based series,¹⁸ and high leakage current for BFO-based series.¹⁹ KNN-based piezoceramics have therefore developed into the most promising competitor to the lead-based ones because of their superior piezoelectric performance and high Curie temperature, especially after the progress of phase boundary engineering. In 2004, Saito *et al.*²⁰ reported on the revolutionary piezoelectricity ($d_{33} \sim 416$ pC/N) on Li/Ta/Sb comodified textured KNN-based piezoceramics with a polymorphic phase boundary (PPB). Superior piezoelectric properties ($d_{33} > 550$ pC/N) in the multiphase coexistence in the KNNS-BZ-BKH ternary system were also obtained by Xu *et al.*²¹ Though phase boundary engineering has made outstanding progress in improving the piezoelectric performance of KNN-based ceramics, their applications on high-sensitive ultrasonic transducer are a few of the remaining concerns. In 2009, Wu *et al.*²² reported an ultrasonic transducer with an insertion loss of 18 dB based on a KNLNT piezoceramic. In 2015, Bah *et al.* reported an undoped-KNN ceramic transducer with an insertion loss of 27 dB.²³ Nevertheless, their sensitivity is still slightly less impressive compared to that of lead-based series. Therefore, further research is desired to develop novel high-frequency lead-free transducers with higher sensitivity based on modified KNN-based piezoelectric materials. Recently, we reported a highly sensitive ultrasonic transducer based on a novel KNN-NTK-FM lead-free piezoceramic.²⁴ It exhibited very promising and comparable low insertion loss to the lead-free ultrasonic transducers.

Piezoelectric 1-3 composites provide many advantages over conventional monolithic piezoelectric ceramics and single crystals, including lower acoustic impedance, lower mechanical and electric loss, and higher electromechanical coupling coefficient (k_t).^{25–28} By properly selecting the bulk ceramics, polymer, and their volume fractions, the performance of the piezocomposite can be optimized to meet specific requirements. As a result, 1-3 piezocomposites have been broadly applied in ultrasonic transducers for biomedical imaging applications.^{26,29} Hence, there is a need to develop lead-free KNN-based piezocomposite transducers that can operate efficiently at high frequencies.

In this study, a new microscale lead-free 1-3 piezocomposite based on a phase boundary-engineered (K_{1-x}Na_x)NbO₃-based ceramic was developed. The fabricated piezocomposite was employed as the active piezoelectric element to fabricate highly sensitivity ultrasonic transducers for biomedical imaging applications. Performance of the 1-3 piezocomposite and as-fabricated transducers was evaluated and characterized. A high center frequency (16 MHz), a broad -6 dB bandwidth (83%), and a very low insertion loss (9.8 dB) were obtained, indicating the developed 1-3 piezocomposite exhibits quite a potential as a substitute for lead-based materials in fabricating environmentally friendly high-sensitivity ultrasonic transducers for biomedical imaging application.

II. MATERIALS AND METHODS

A. Preparation and characterizations of the Fe-KNN-based lead-free piezoceramic

A (K_{1-x}Na_x)NbO₃-(Bi_{1-x}Na_x)ZrO₃-BiScO₃ (Fe-KNN-based) ternary system piezoelectric ceramic with Fe₂O₃-added was synthesized via the solid-state reaction technique, as described elsewhere.¹⁵ To determine the crystal structure of the sintered ceramic, the Rietveld refinement supported by the Fullprof program on X-ray diffraction (XRD) pattern was investigated by using *P4mm* (ICSD-9532) and *Amm2* (ICSD-9533) atomic coordinates as the initial models. In Fig. 1(a), measured and calculated diffraction profiles, and the difference curves, are presented. A typical perovskite structure with a multiphase coexisting state (tetragonal and orthorhombic) can be identified. The difference curve (green line) reveals that the refined profile fit well with the experimental one. The error factors (e.g., $R_p = 10.9\%$, $R_{wp} = 7.97\%$, $R_{exp} = 6.04\%$, and $\chi^2 = 1.73$) are limited to an acceptable range. The detailed structural parameters of the refinement result are summarized in Table S1 (see the supplementary material). The multiphase structure can be further determined through the temperature dependence of the permittivity spectrum. As shown in Fig. 1(b), a permittivity anomaly (around 50 C) was observed, corresponding to the orthorhombic-tetragonal (O-T) phase transition temperature. Therefore, combined with both the XRD Rietveld refinement and permittivity spectrum, we propose that the main phase of the Fe-KNN-based piezoceramic has a *P4mm* tetragonal structure and an *Amm2* orthorhombic structure simultaneously. The spontaneous polarization directions in orthorhombic and tetragonal phases change across the orthorhombic-tetragonal phase boundary owing to the [110] and [100] polarizations, respectively. Figures 1(c) and 1(d) show the SEM images and elemental mapping of the sintered Fe-KNN-based ceramic sample. Voids were hardly observed and the elements are homogeneously distributed, indicating a uniform and dense ceramic microstructure.

B. Design and fabrication of the 1-3 ceramic/polymer piezocomposite

In designing the spatial scale of a 1-3 piezocomposite, there are several guidelines to follow to improve transducer performance.³⁰ First, a width-to-thickness aspect ratio of the piezoelectric pillar less than 0.5 is required because the half-wave lateral mode of the elements should be above the fundamental thickness vibration so that their harmonics do not couple to the thickness mode.^{31,32} Second, the stopband edge resonant frequency should be higher than twice the fundamental thickness resonant frequency, which provides the conditions for the piezocomposite design as follows:^{25,27}

$$s < \frac{v_s}{4f}, \quad w < \frac{v_l}{4f}, \quad f_l = \frac{v_s}{2\sqrt{2}s}, \quad \text{and} \quad f < \frac{f_l}{2}, \quad (1)$$

where s is the kerf width, v_s is the shear wave velocity in the polymer fillers, f is the thickness mode resonant frequency of the piezocomposites, w is the lateral width of piezoelectric pillar, v_l is the lateral wave velocity of the piezoelectric pillar, and f_l is the frequency of the first lateral mode, respectively. The higher frequency is

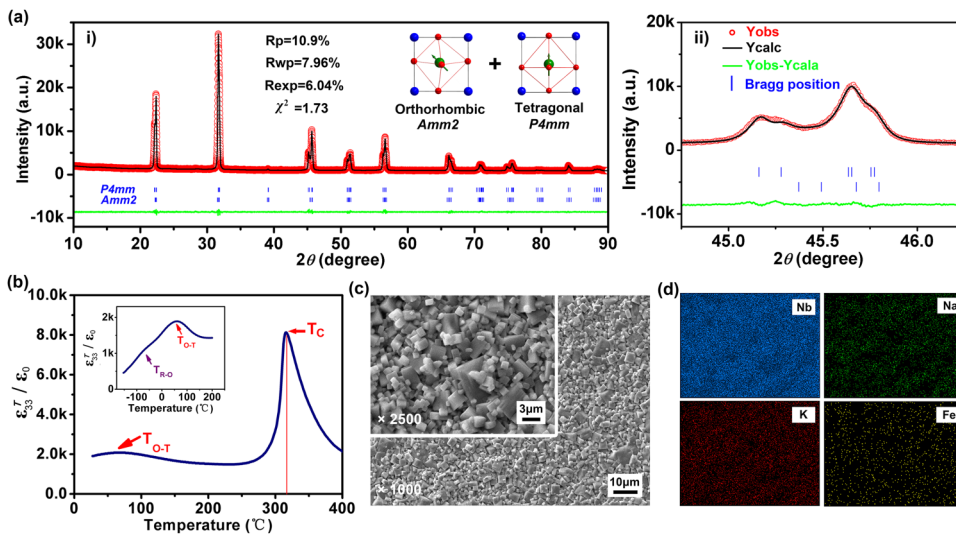


FIG. 1. (a) Rietveld refinement on XRD pattern, (b) temperature dependence of the permittivity spectrum, (c) SEM micrographs, and (d) element mapping of the Fe-KNN-based ceramic.

designed, the smaller kerf is required while ensuring the integrity of ceramic pillars. Therefore, a modified technique that employs a small size blade and multiple dice-and-fill processes was used to fabricate a microscale 1-3 ceramic/polymer piezocomposite formed by regular-shaped pillar arrays and small kerfs, as illustrated in Fig. 2. Additionally, the performance of the piezocomposite can be calculated theoretically as a function of volume fraction (v) according to the modified parallel and series model [see Fig. 3(a)].³³ Based on the above analysis and the actual width of the dicing blade, a ceramic/polymer 1-3 piezocomposite with the miniaturized lateral width ($55 \times 55 \mu\text{m}^2$) and kerfs ($15 \mu\text{m}$) was designed and fabricated [see Fig. 3(b)], which satisfies an optimized ceramic volume fraction ($\sim 62\%$). An insulating epoxy (EPO-TEK 301) (see Table S2 in the supplementary material for the properties of the resin) was applied to fill into the kerfs. Optical images of the Fe-KNN-based ceramic rods array after dicing are demonstrated in Figs. 4(a) and 4(b). A summary of some important piezoelectric and acoustic parameters of the ceramic/polymer 1-3 piezocomposite and some other representative piezo-materials are listed in Table I. The detailed calculation and measurement methods are provided in Sec. S1 of the supplementary material.

C. Design and fabrication of transducers

Based on the above 1-3 piezocomposite, an 18 MHz ultrasonic transducer with an active aperture size of $\varnothing 2.7 \text{ mm}$ was further designed and fabricated. A piezoelectric transducer modeling software (PiezoCAD) based on Krimboldz, Leedom, and Mattaei (KLM) equivalent circuit model was employed to optimize design of the transducer. To improve bandwidth of the transducer, two matching layers with thickness of quarter wavelength were applied to compensate acoustic impedance mismatch between the 1-3 piezocomposite ($Z_a = 12.1 \text{ MRayl}$) and the biological tissues (1.5 MRayl). A silver loaded epoxy (7.3 MRayl) made from a mixture of Insulcast 501, Insulcure 9 (American Safety Technologies, Roseland, NJ), and $2\text{--}3 \mu\text{m}$ silver powder (Sigma-Aldrich Inc.) was used as the first

matching layer. A parylene C dimer (DPX-C, Specialty Coating Systems) was applied as the second matching layer ($Z \sim 2.5 \text{ MRayl}$). A commercial conductive silver paste (E-solder 3022, Von Roll Isola) ($Z \sim 5.9 \text{ MRayl}$) was employed as the backing material. The manufacturing process is described as follows: First, the prepared 1-3 piezocomposite was lapped down to a thickness of $110 \mu\text{m}$, which was determined by the following equation:

$$t = \frac{C_p}{2f}, \quad (2)$$

where C_p is the acoustic velocity. A Cr/Au (50/100 nm) electrode was sputtered on both sides of the lapped 1-3 piezocomposite. Next,

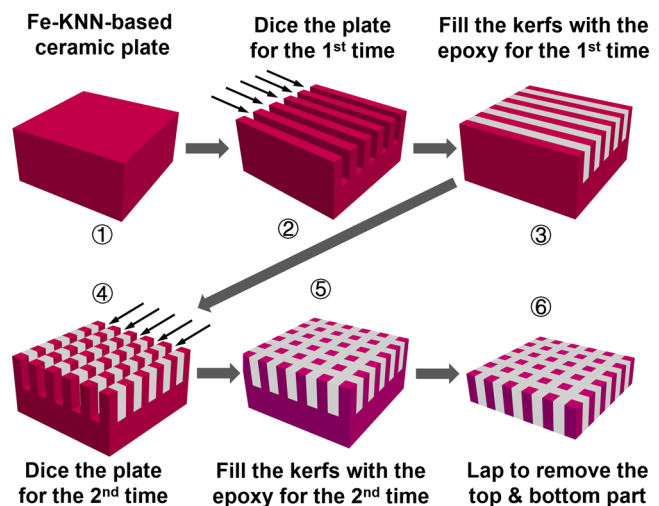


FIG. 2. Schematic illustration of the modified dice-and-fill method used for Fe-KNN-based 1-3 piezocomposite fabrication.

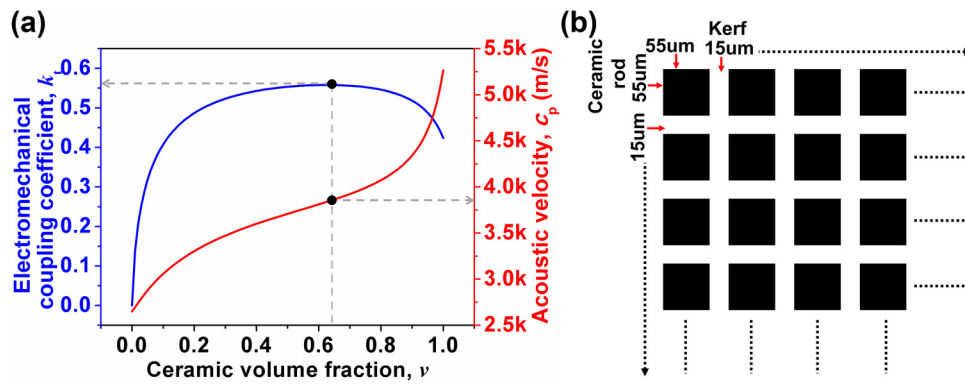


FIG. 3. (a) Electromechanical coupling coefficient k_t and acoustic velocity c_p of the 1-3 piezocomposites calculated as a function of ceramic volume fraction. (b) Schematic illustration of the 1-3 piezocomposite design with miniaturized ceramic rods of lateral width of 55 μm and kerfs of 15 μm .

the first matching layer and backing materials were deposited onto the corresponding sides of the piezocomposite. After curing, the matching layer and backing material were lapped down to 30 μm and 3 mm [see Figs. 4(c) and 4(d)], respectively. To meet electrical impedance matching between the device and electrical terminations (usually 50 Ω), the whole piezoelectric stack was diced into small square posts then machined into circular disks on a lathe with a diameter of \varnothing 2.7 mm, which can be estimated using the following equation:

$$Z_e = \frac{t}{2\pi\omega A\epsilon^S}, \quad (3)$$

where t and ϵ^S are the thickness and permittivity of the piezocomposite, respectively. The matched and backed acoustic stack was then inserted and fixed into a brass housing. A subminiature version A (SMA) connector was connected with the conductive backing via a lead wire. Another Cr/Au (50/100 nm) electrode was sputtered across the first matching layer and the brass housing to form a common ground connection. Finally, a 30 μm thick parylene was deposited onto the entire external surface of the device as the second matching layer and the protective layer. Design parameters of the 1-3 piezocomposite device are summarized in Table II. Structure schematic is illustrated in Fig. 4(e) (left). Photographs of the as-fabricated transducers are shown in Fig. 2(e) (right).

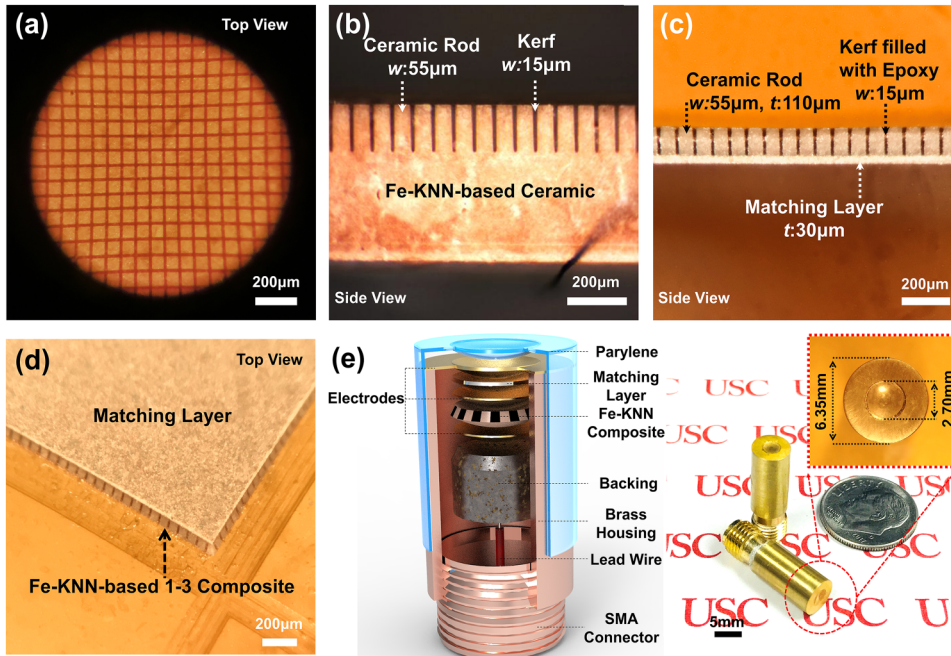


FIG. 4. (a) and (b) Optical images of the Fe-KNN-based ceramic rods array after dicing. (c) and (d) Optical images of the as-developed 1-3 piezocomposite sample with a matching layer after lapping to the required thickness. (e) Schematic illustration of the inner structures (left) and photographs of as-fabricated samples (right) of the Fe-KNN-based 1-3 piezocomposite transducers; the inset shows the optical image of the front end of the transducer.

TABLE I. The acoustic and electrical properties of the Fe-KNN-based 1-3 piezocomposite and some other representative piezoelectric materials.

Materials	ρ (kg/m ³)	Z_a (MRayl)	d_{33} (pC/N)	ϵ^s/ϵ_0	k_t	c_p (m/s)	T_c (C)	$\tan \delta$ (%)
PMN-PT single crystal ³⁴	8060	37.1	2820	680–800	0.58	4610	130	0.4
PZT-5H ceramic ³⁵	7500	30	593	1470	0.51	4580	200	2.0
BZT-50BCT ceramic ³⁶	5200	26.7	597	2817	0.41	5133	93	2.0
Undoped KNN ceramic ²³	4030	23	N/A	125	0.46	5700	N/A	6.0
KNLNT ceramic ²²	4544	31	245	890	0.42	6875	N/A	4.5
KNN-NTK-FM ²⁴	4540	28.5	324	926	0.44	6270	304	2.2
Fe-KNN-based 1-3 piezocomposite (this work)	3103	12.1	340	513	0.59	3889	317	3.0

III. RESULTS

A. Transducer basic performance evaluation

The PiezoCAD impedance spectrum and pulse-echo response simulation results of the designed Fe-KNN-based 1-3 piezocomposite transducer as comparison are demonstrated in Figs. 5(a) and 5(b), respectively. As presented in Fig. 5(c), the actual impedance magnitude and phase angle of the 1-3 piezocomposite transducer was characterized by an impedance analyzer (HP 4294A, Agilent). The thickness mode resonance frequency (f_r) and antiresonance frequency (f_a) of the piezocomposite transducer are located at 19.6 and 23.5 MHz, respectively. According to the IEEE standard,³⁷ the effective electromechanical coupling coefficient (k_{eff}) of a device, describing the conversion efficiency between electrical energy and mechanical energy, was formulated by

$$k_{\text{eff}} = \sqrt{1 - \frac{f_r^2}{f_a^2}}, \quad (4)$$

where k_{eff} for the piezocomposite transducer is calculated to be 0.55, which is much higher than that (0.45) of the previous reported ultrasonic transducer based on the KNN-NTK-FM lead-free ceramic.²⁴ The result indicates that the fabricated 1-3 piezocomposite transducer exhibits a better performance.

Time domain pulse-echo responses [see Fig. 5(d)] and the insertion loss (see Fig. 6) of the 1-3 piezocomposite transducer were measured using the same procedures described in our

previous work.²⁴ The center frequency (f_c) of the 1-3 piezocomposite transducer was calculated to be 16 MHz and the –6 dB bandwidth was 83%. The measured result is in good agreement with the PiezoCAD simulation [see Fig. 5(b)]. Figure 6 demonstrates the insertion loss (IL) as a function of frequency (5–35 MHz) of the 1-3 piezocomposite transducer, which was evaluated by

$$IL = \left| 20 \log \frac{V_o}{V_i} + \alpha_{\text{water}} \cdot 2d \cdot f^2 + 1.9 \right|, \quad (5)$$

where the final IL value was compensated with the losses produced by the attenuation of water path (the distance both ultrasound wave and echo traveled through the water between the transducer and the quartz target) [$\alpha_{\text{water}} = 2.2 \times 10^{-4} \text{ dB} \cdot (\text{mm MHz}^2)^{-1}$] and the diffraction of the quartz target (1.9 dB).³⁸ The lowest insertion loss for the 1-3 piezocomposite transducer was found at 19 MHz with only 9.8 dB. The results indicate the piezocomposite transducer exhibits an extremely high-sensitivity.

B. Transducer imaging performance evaluation

Imaging is the ultimate test of an ultrasonic transducer performance. We employed an ultrasonic biomicroscope (UBM) system (see Fig. 7) described in our previous work²⁴ for a series of imaging tests including wire phantom imaging and *ex vivo* porcine eyeball imaging using the Fe-KNN-based 1-3 piezocomposite transducer.

One important metric of ultrasonic imaging is the spatial resolution in both lateral and axial directions. In theory, the –6 dB axial resolution (R_{axial}) can be evaluated by the following formula:

$$R_{\text{axial}} = \frac{\lambda}{2 \times BW}, \quad (6)$$

where λ is the wavelength of the ultrasound in the water, and BW is the bandwidth of the transducer. For the as-fabricated 16 MHz transducer, the theoretical axial resolution was estimated to be 58 μm . The lateral resolution (R_{lateral}) is mainly dependent on device geometry, which can be estimated by

$$R_{\text{lateral}} = \lambda \times f. \quad (7)$$

The f -number is used to describe the ratio between the focal length and the aperture size. To comprehensively explore the

TABLE II. Design parameters of the Fe-KNN-based 1-3 piezocomposite transducer.

Specifications	1-3 piezocomposite transducer
Designed center frequency	18 MHz
Aperture size	\varnothing 2.7 mm
Electrical impedance	50 Ω
Thickness of the piezoelectric material (1-3 piezocomposite)	110 μm
Thickness of the 1st matching layer (2–3 μm silver loaded epoxy)	30 μm
Thickness of the 2nd matching layer (Parlylene)	35 μm
Thickness of backing (E-solder 3022)	3 mm

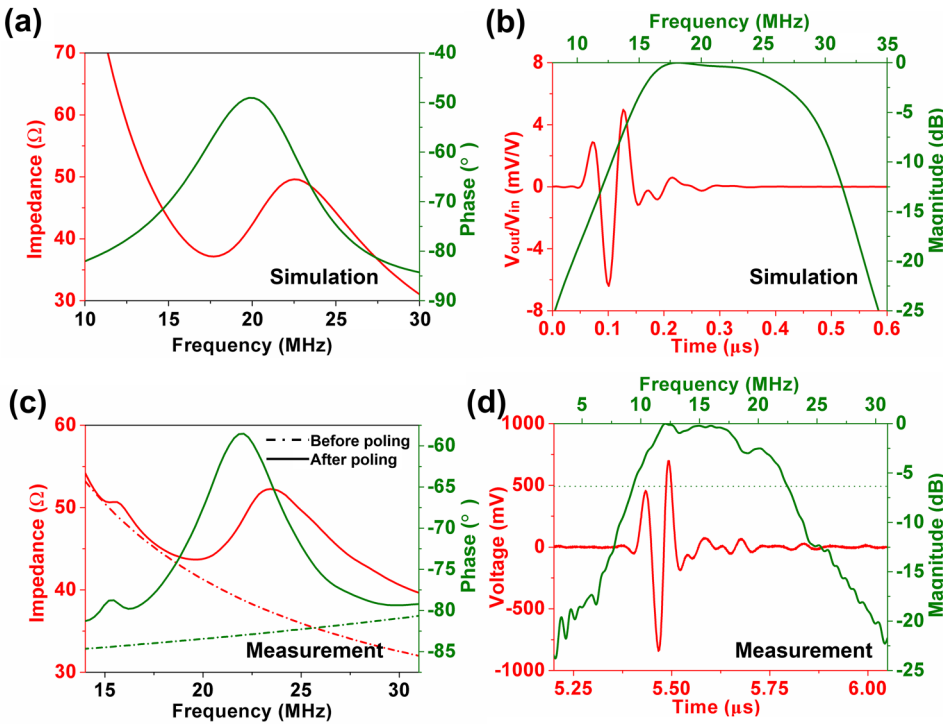


FIG. 5. (a) Simulated electrical impedance magnitude (red) and phase (green), (b) simulated pulse-echo waveform (red) and its frequency spectrum (green), (c) measured electrical impedance magnitude (red) and phase (green) before (dotted) and after (solid) poling, and (d) measured pulse-echo waveform (red) and its frequency spectrum (green) of the Fe-KNN-based 1-3 piezocomposite transducer.

imaging capabilities of transducers with different lateral resolutions, three different *f*-number (1.5, 2, and 2.5) transducers were obtained by hot pressing (see Fig. S3, [supplementary material](#)), the theoretical lateral resolutions of which were estimated to be 144, 193, and 241 μm , respectively. The actual lateral and axial resolutions of these transducers were evaluated by imaging a wire phantom consisting of three tungsten wires of 15- μm in diameter (California Fine Wire Co.). As demonstrated in Fig. 8(b), three wires settled in parallel with increased distance (0.15, 0.25, and

0.5 mm) in the lateral direction and equal distance (1 mm) in the axial direction. Figures 8(b)–8(d) display the images obtained by the three transducers with *f*-number of 1.5, 2.0, and 2.5. The line spread functions in both directions, shown in Figs. 9(a)–9(c), were extracted from the first wire in the phantom (located about 4 mm away from the transducer with *f*-number of 1.5, 5.5 mm away from the transducer with *f*-number of 2.0, and 6.5 mm away from the transducer with *f*-number of 2.5, respectively). The –6 dB axial and lateral resolutions for the three transducers with

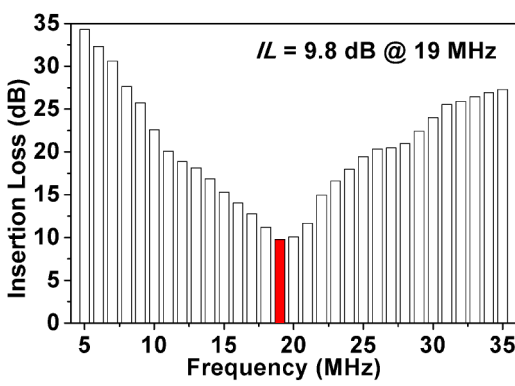


FIG. 6. Measured insertion-loss of the Fe-KNN-based 1-3 piezocomposite transducer.

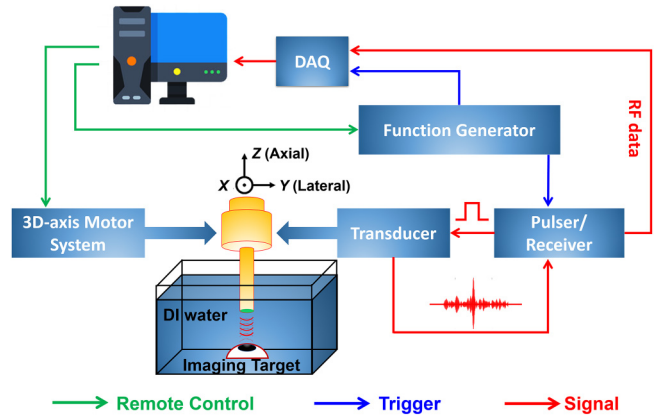


FIG. 7. Schematic illustration of an ultrasonic biomicroscope (UBM) system.²⁴

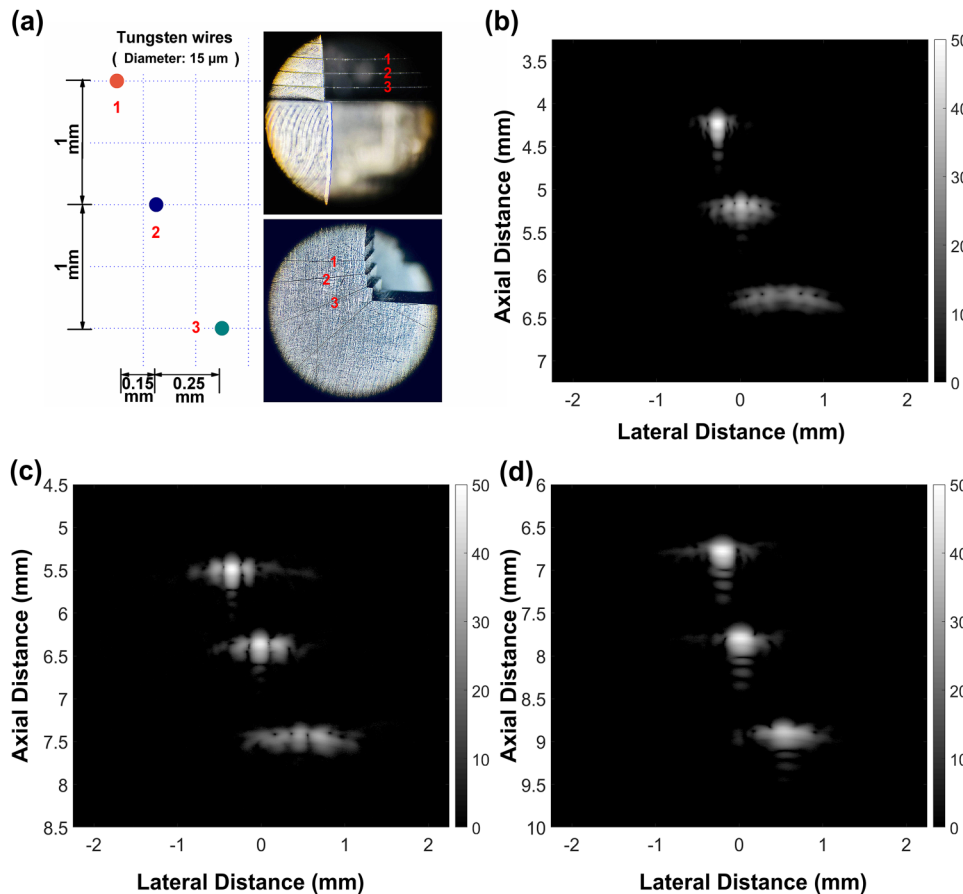


FIG. 8. (a) Arrangement of a wire phantom comprised of three tungsten wires of diameter $15\text{ }\mu\text{m}$. Wire phantom UBM images produced by three Fe-KNN-based 1-3 piezocomposite transducers with *f*-number of (b) 1.5, (c) 2.0, and (d) 2.5 (dynamic range: 50 dB).

f-number of 1.5, 2.0, and 2.5 were measured to be 226 and $239\text{ }\mu\text{m}$, 227 and $599\text{ }\mu\text{m}$, and 226 and $413\text{ }\mu\text{m}$, respectively, which are in good agreement with theoretical predictions. The lateral resolution anomaly ($599\text{ }\mu\text{m}$) for the transducer with *f*-number of 2.0 may be caused by the rupture of the piezoelectric layer when the transducer was press focused by a highly polished steel ball bearing.

Finally, the ability of the Fe-KNN-based 1-3 piezocomposite transducers to image biological tissues was evaluated by imaging an excised porcine eyeball. Field of view (FOV) of imaging was set according to the focusing ability of the transducers to image the entire anterior portion of a porcine eyeball. Figure 10 shows the UBM images by using three Fe-KNN-based 1-3 piezocomposite transducers with different *f*-number (1.5, 2.0, and 2.5) [Figs. 10(a)-10(c)]. Eyeball anatomical details including the cornea (C1), conjunctiva (C2), ciliary body (C3), iris (I), the surface of lens (L1), limbus (L2), and sclera (S) are more clearly visualized in Fig. 10(a). The results demonstrate that, on the one hand, the one with a small *f*-number (1.5) among the three piezocomposite transducers has better imaging capabilities. On the other hand, transducers using the 1-3 piezocomposite exhibit enhanced imaging sensitivity over the previous transducer based on pure ceramic.²⁴

IV. DISCUSSION

In this study, a phase boundary-engineered Fe-KNN-based lead-free piezoceramic was utilized to design and manufacture 1-3 piezocomposite for high-sensitivity ultrasound transducers applications. The as-fabricated piezocomposite transducer possesses an enhanced effective electromechanical coupling factor k_{eff} (0.55), a wide bandwidth (83%), and an ultra-low two-way insertion loss (9.8 dB). As listed in Table III, the insertion loss of the Fe-KNN-based 1-3 piezocomposite transducer, as far as we know, is the lowest compared to previous reported lead-free transducers, indicating that the transducer made from the Fe-KNN-based 1-3 piezocomposite exhibits a much better sensitivity than the other lead-free transducers.

First, the high sensitivity can be attributed in part to the internal phase boundary structure [see Figs. 1(a) and 1(b)] of Fe-KNN-based lead-free piezoceramic rods. Phase boundary engineering exploited to construct multiphase coexistence regions in potassium-sodium niobate-based materials that resembles the morphotropic phase boundary (MPB) in lead zirconate titanate has proven to be highly successful in improving the electrical performance.^{8,45} For multiple phases coexisting ceramic materials, polymorphic phase boundary (PPB) structure facilitates polarization rotation between two nearly

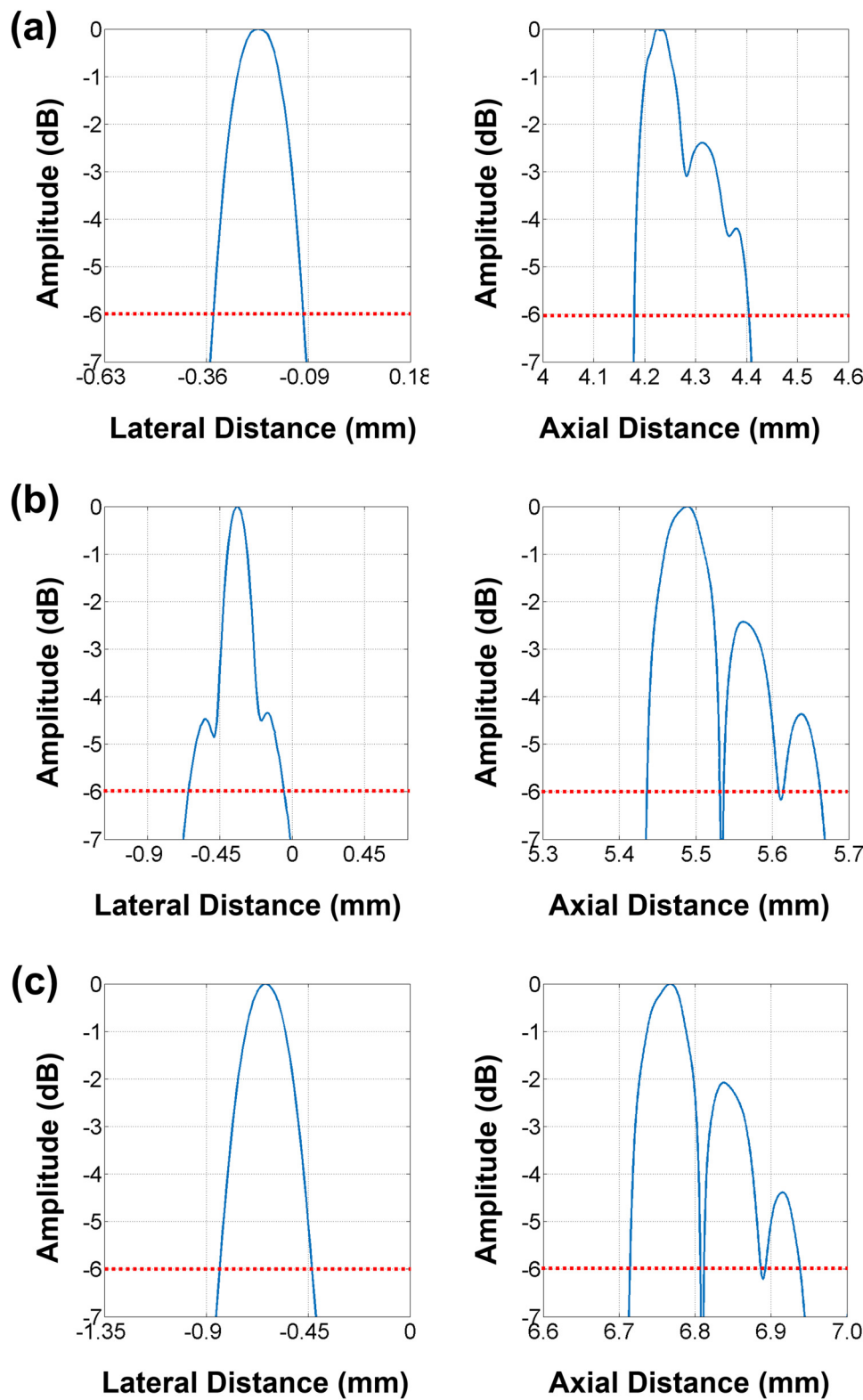


FIG. 9. Lateral and axial line spread functions of the first wire in the wire phantom produced by three Fe-KNN-based 1-3 piezocomposite transducers with f -number of (a) 1.5, (b) 2.0, and (c) 2.5.

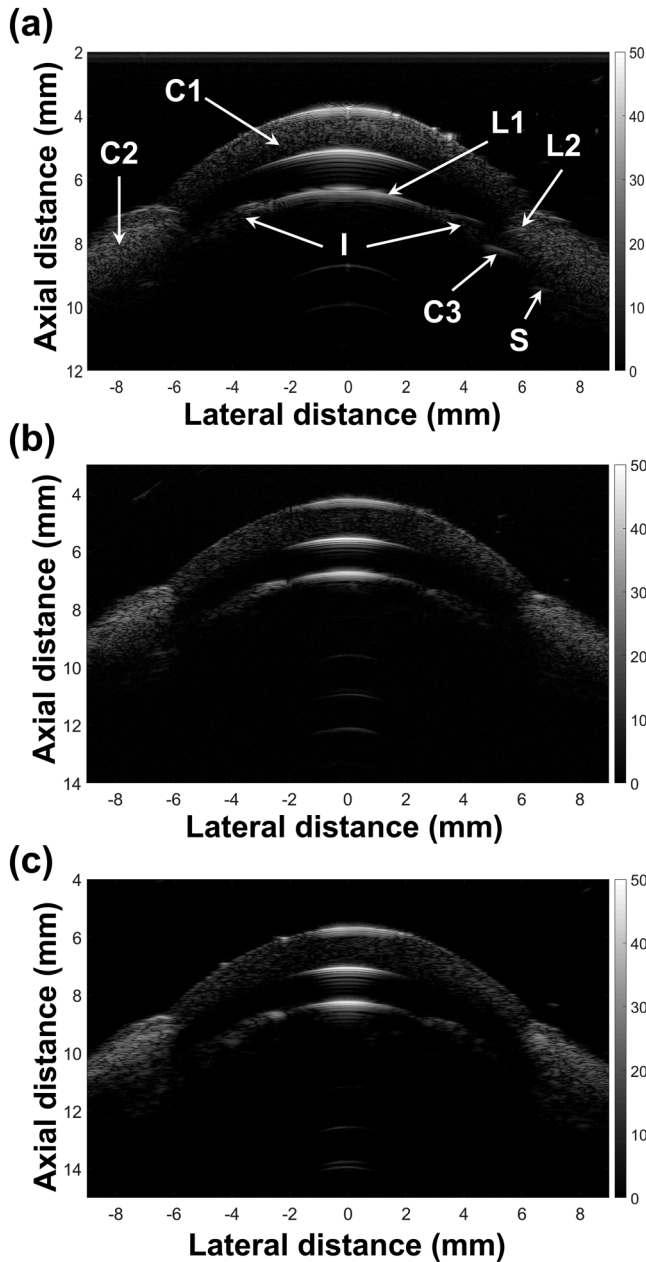


FIG. 10. UBM imaging of the anterior portion in an excised porcine eyeball using three Fe-KNN-based 1-3 piezocomposite transducers with f -number of (a) 1.5, (b) 2.0, and (c) 2.5 (dynamic range: 50 dB, C1: cornea, C2: conjunctiva, C3: ciliary body, I: iris, L1: lens, L2: limbus, S: sclera).

energetically degenerate phases in the ceramic because of the greater number of possible crystallographic orientations.⁴⁶

Second, as discussed previously, a piezocomposite combining the desirable performance of two different phases might be superior. The idea has proven to be quite successful in developing 1-3

TABLE III. Performance comparison of the ultrasonic transducers prepared using the 1-3 piezocomposite and other piezoelectric materials.

Piezoelectric materials	f_c (MHz)	-6 dB BW (%)	IL (dB)
Mn-KNN single crystal ³⁹	51.8	70.2	91.2
KNNS-BNKZ ceramic ⁴⁰	37	56.8	16
Undoped KNN ceramic ²³	5.5	49	27
KNN-NTK-FM ceramic ²⁴	52.6	64.4	10.1
1-3 KNN-based piezocomposites ⁴¹	29	90	25.1
PIN-PMN-PT single crystal ⁴²	35; 60	48; 47	15; 17
Modified PMN-PT ceramic ⁴³	39	80	13
LiNbO_3 single crystal ⁴⁴	45	74	21.3
BZT-50BCT ceramic ³⁶	30.5	53	18.7
Fe-KNN-based 1-3 piezocomposite (this work)	16	83	9.8

piezocomposite composed of piezoelectric rod array and piezoelectric inactive polymer.²⁵ In this work, the 1-3 piezocomposite comprises a system of phase boundary-engineered ceramic rod array in the shape of parallelepipeds with square bases and the insulating polymer filler [refer to the schematic shown in Fig. 11(a)]. These ceramic rods are continuous in the x_3 direction, and their lateral faces are parallel to the (x_1x_3) and (x_2x_3) planes. It is supposed that each multiphase coexistence ceramic rod poled along the [001] and [110] directions is split into domains with polarization vectors $P_{s,1}$, $P_{s,2}$, $P_{s,3}$, and $P_{s,4}$.⁴⁷ The ceramic elements are regularly arranged in the polymer matrix such that the centers of symmetry of the rod base forms a simple square lattice in the (x_1x_2) plane. In this design of the 1-3 ceramic/polymer piezocomposite, the main goal is to lower the permittivity and decouple the transverse piezoelectric coefficient d_{31} to enhance the hydrostatic voltage coefficient g_h ($d_h/\epsilon_0\epsilon_r$) and hydrostatic piezoelectric factor d_h ($d_{33} + 2d_{31}$). The vibration for each piezoceramic rod is dominant in the fundamental length longitudinal 3-3 direction with a higher efficiency determined by the piezoelectric coupling factor k_{33} . An ultrasonic transducer is a device that converts electrical energy into acoustic energy and vice versa through piezoelectricity or electrostriction. For example, in the biomedical imaging applications, a transducer piezoelectric layer not only produces ultrasound into a given medium but also senses the weak echoes reflected, in the so-called pulse-echo mode.⁴¹ Although pure ceramic disk exhibits a high piezoelectric coefficient d_{33} , the piezoelectric voltage coefficient g_{33} is low due to the high permittivity. Thus, pure ceramic layer is not a good receiver for ultrasound. The idea of piezocomposite transducers inspires us to design a 1-3 ceramic/polymer structure to augment the g_{33} (d_{33}/ϵ_{33}^T) factor and thus optimize the sensitivity in the receiving mode.²⁵ If the receiving voltage sensitivity is improved, the organism can be interrogated under lower acoustic energy and the ultrasonic biological effects can be minimized. In this work, g_{33} increases from 23.5×10^{-3} to $34.9 \times 10^{-3} \text{ V m N}^{-1}$, effectively enhancing the sensitivity in the receiving mode for the piezocomposite transducer. In the receiving mode, the piezocomposite can be viewed as consisting of parallel-connected oscillator array. Driven by pulse-echo pressure, all the oscillators vibrate

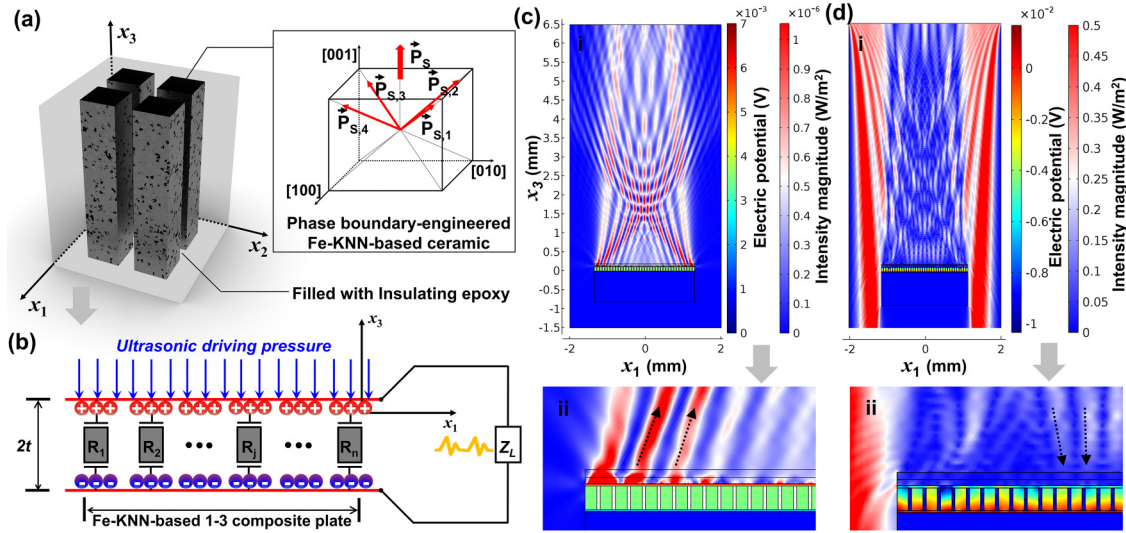


FIG. 11. (a) Schematic illustration of the 1-3 piezocomposite with the planar microgeometry; inset shows the perovskite unit cell with split spontaneous polarization vectors. (b) The equivalent circuit model when the 1-3 piezocomposite acts as an ultrasound receiver. (c) and (d) Simulation results showing the acoustic field and piezoelectric potential distribution when the 1-3 piezocomposite acts as an ultrasound transmitter and receiver, respectively.

along the longitudinal 3–3 direction. The equivalent circuit for the receiver model is demonstrated in Fig. 11(b). The impedance for the oscillator unit R_j can be determined as

$$z_j = -\frac{1}{i\omega C_0} \frac{\xi t \cot(\xi t) - k_{33}^{-2}}{\xi t \cot(\xi t)}, \quad (8)$$

where $C_0 = \frac{\varepsilon_{33} S_j}{2t}$, $k_{33}^{-2} = \frac{e_{33}^2}{\varepsilon_{33} C_{33}}$, $\xi^2 = \frac{\rho}{C_{33}} \omega^2$, and $\bar{C}_{33} = C_{33} \left(1 + \frac{e_{33}^2}{\varepsilon_{33} C_{33}}\right)$. C_0 is the capacitance. c_{33} , e_{33} , and ε_{33} are the effective elastic, piezoelectric, and dielectric constants of the piezocomposite, respectively. ρ , ω , and ξ are the density, angular frequency, and wave number, respectively. t_j and S_j are the thickness and area of the oscillator unit R_j , respectively. The total impedance of the 1-3 piezocomposite plate \bar{Z} can be determined as

$$\frac{1}{\bar{Z}} = \sum_{j=1}^n \frac{1}{Z_j}. \quad (9)$$

The oscillator array can be viewed as electric sources. Thus, the electric potential V applied to the load Z_L can be derived as

$$V = \sum_{j=1}^n I_j Z_L = \frac{Phk_{33}^{-2}}{e_{33}} \sum_{j=1}^n \frac{Z_L}{(Z_j + Z_L)\xi t \cot(\xi t)}. \quad (10)$$

In this above mode, the surface of the piezocomposite is driven by time-harmonic surface normal stress T_{33} ($=Pe^{i\omega t}$), wherein the time-harmonic factor $e^{i\omega t}$ has been reduced to simplicity.^{48,49}

Based on the above analysis and discussion, simulations for the 1-3 piezocomposite acting as an ultrasound transmitter and receiver were performed by the finite element analysis (FEA)

technique using COMSOL Multiphysics package, as demonstrated in Figs. 11(c) and 11(d). In the simulation, the considered physics fields were pressure acoustics (frequency-domain), solid mechanics, electrostatics, piezoelectric effect and acoustic-structure boundary. The piezoelectric material's parameters were set according to the experimentally measured properties listed in Table I. The geometry of piezocomposite and the matching layer's parameters in the simulation were strictly consistent with the designs of the 1-3 type ceramic/polymer piezocomposite and the transducer shown in Materials and Methods. Other materials were chosen from COMSOL's material library. To ensure the validity and accuracy of our simulation results, the mesh size is set from 0.002 mm to 0.01 mm, which is smaller than $\lambda/7$, with a growth rate of 1.3. Given the conditions that wave propagation distance was only 6.5 mm and the background medium was water which has an attenuation coefficient of $2.2 \times 10^{-4} \text{ dB} \cdot (\text{mm MHz})^{-1}$,³⁸ damping was considered negligible and was not included in the simulation. The value of acoustic intensity magnitude and piezoelectric potential distribution into the piezocomposite layer are indicated by the color bar. It can be seen from the results of the FEA that the 1-3 piezocomposite transducer can convert considerable acoustic output from electricity, and vice versa.

V. CONCLUSION

In conclusion, we have introduced the design and fabrication of the newly microscale Fe-KNN-based lead-free 1-3 piezocomposite and its application on ultrasound imaging transducers. A modified dice-and-fill fabrication technique was employed to building the microscale piezocomposite, by which the lead-free piezoceramic rods were miniaturized to a lateral width of $55 \mu\text{m}$ with kerfs of $15 \mu\text{m}$. The fabricated transducers using the piezocomposite exhibit

improved performance with an enhanced effective electromechanical coupling coefficient k_{eff} (0.55) and an ultra-low two-way insertion loss (9.8 dB), which inspires further research on the use of the KNN-based 1-3 piezocomposite in the next generation high-sensitivity ultrasonic imaging transducers that require environment-friendly materials.

SUPPLEMENTARY MATERIAL

See the [supplementary material](#) for the Rietveld refinement parameters, theoretical calculation of composite, and hot-pressing process of transducer focusing.

ACKNOWLEDGMENTS

This work was supported in part by the National Institutes of Health (NIH) under Grant Nos. 1R01EY026091, R01 EY028662, and R01 HL127271, and an Unrestricted Grant to the Department of Ophthalmology from Research to Prevent Blindness, New York, NY. The work of L. Jiang was supported by the National Natural Science Foundation of China (NNSFC) (Grant No. 51332003) and China Scholarship Council (File No. 201706240056).

REFERENCES

- ¹F. S. Foster, C. J. Pavlin, K. A. Harasiewicz, D. A. Christopher, and D. H. Turnbull, *Ultrasound Med. Biol.* **26**, 1–27 (2000).
- ²H. Hu, X. Zhu, C. Wang, L. Zhang, X. Li, S. Lee, Z. Huang, R. Chen, Z. Chen, and C. Wang, *Sci. Adv.* **4**, eaar3979 (2018).
- ³K. K. Shung, J. Cannata, and Q. Zhou, *J. Electroceram.* **19**, 141–147 (2007).
- ⁴K. K. Shung, *Diagnostic Ultrasound: Imaging and Blood Flow Measurements* (CRC Press, 2015).
- ⁵Q. Zhou, S. Lau, D. Wu, and K. K. Shung, *Prog. Mater. Sci.* **56**, 139–174 (2011).
- ⁶Q. Zhou, K. H. Lam, H. Zheng, W. Qiu, and K. K. Shung, *Prog. Mater. Sci.* **66**, 87–111 (2014).
- ⁷D. Damjanovic and G. A. Rossetti, *MRS Bull.* **43**, 588–594 (2018).
- ⁸J. Wu, D. Xiao, and J. Zhu, *Chem. Rev.* **115**, 2559–2595 (2015).
- ⁹J. Rödel, W. Jo, K. T. Seifert, E. M. Anton, T. Granzow, and D. Damjanovic, *J. Am. Ceram. Soc.* **92**, 1153–1177 (2009).
- ¹⁰M. Pecht, Y. Fukuda, and S. Rajagopal, *IEEE Trans. Electron. Packag. Manuf.* **27**, 221–232 (2004).
- ¹¹L. Jiang, J. Xing, Z. Tan, J. Wu, Q. Chen, D. Xiao, and J. Zhu, *J. Mater. Sci.* **51**, 4963–4972 (2016).
- ¹²J. F. Li, K. Wang, F. Y. Zhu, L. Q. Cheng, and F. Z. Yao, *J. Am. Ceram. Soc.* **96**, 3677–3696 (2013).
- ¹³J. Xing, Z. Tan, L. Jiang, Y. Wu, Y. Yue, Q. Chen, J. Wu, W. Zhang, D. Xiao, and J. Zhu, *Appl. Phys. Lett.* **110**, 022905 (2017).
- ¹⁴J. Xing, Z. Tan, J. Yuan, L. Jiang, Q. Chen, J. Wu, W. Zhang, D. Xiao, and J. Zhu, *RSC Adv.* **6**, 57210–57216 (2016).
- ¹⁵L. Jiang, Z. Tan, L. Xie, Y. Li, J. Xing, J. Wu, Q. Chen, D. Xiao, and J. Zhu, *J. Eur. Ceram. Soc.* **38**, 2335–2343 (2018).
- ¹⁶M. H. Lee, D. J. Kim, J. S. Park, S. W. Kim, T. K. Song, M. H. Kim, W. J. Kim, D. Do, and I. K. Jeong, *Adv. Mater.* **27**, 6976–6982 (2015).
- ¹⁷C. Zhao, H. Wu, F. Li, Y. Cai, Y. Zhang, D. Song, J. Wu, X. Lyu, J. Yin, and D. Xiao, *J. Am. Chem. Soc.* **140**, 15252–15260 (2018).
- ¹⁸W. Bai, L. Li, W. Wang, B. Shen, and J. Zhai, *Solid State Commun.* **206**, 22–25 (2015).
- ¹⁹S. Huang, Q. Li, L. Yang, J. Xu, C. Zhou, G. Chen, C. Yuan, and G. Rao, *Ceram. Int.* **44**, 8955–8962 (2018).
- ²⁰Y. Saito, H. Takao, T. Tani, T. Nonoyama, K. Takatori, T. Homma, T. Nagaya, and M. Nakamura, *Nature* **432**, 84 (2004).
- ²¹K. Xu, J. Li, X. Lv, J. Wu, X. Zhang, D. Xiao, and J. Zhu, *Adv. Mater.* **28**, 8519–8523 (2016).
- ²²D. Wu, R. Chen, Q. Zhou, K. Shung, D. Lin, and H. Chan, *Ultrasonics* **49**, 395–398 (2009).
- ²³M. Bah, F. Giovannelli, F. Schoenstein, C. Brosseau, J.-R. Deschamps, F. Dorvaux, L. Haumesser, E. Le Clezio, and I. Monot-Laffez, *Ultrasonics* **63**, 23–30 (2015).
- ²⁴R. Chen, L. Jiang, T. Zhang, T. Matsuoka, M. Yamazaki, X. Qian, G. Lu, A. Safari, J. Zhu, and K. K. Shung, *IEEE Trans. Biomed. Eng.* **66**, 1580–1587 (2018).
- ²⁵T. Gururaja, W. A. Schulze, L. E. Cross, R. E. Newnham, B. A. Auld, and Y. J. Wang, *IEEE Trans. Sonics Ultrason.* **32**, 481–498 (1985).
- ²⁶D. Fiore, R. Gentilman, H. Pham, W. Serwatka, P. McGuire, and L. Bowen, in *Proceedings of the Tenth IEEE International Symposium on Applications of Ferroelectrics* (IEEE, 1996), Vol. 1, pp. 531–534.
- ²⁷X. Geng and Q. Zhang, *J. Appl. Phys.* **85**, 1342–1350 (1999).
- ²⁸L. Jiang, Y. Yang, R. Chen, G. Lu, R. Li, D. Li, M. S. Humayun, K. K. Shung, J. Zhu, Y. Chen, and Q. Zhou, *Nano Energy* **56**, 216–224 (2019).
- ²⁹R. Liu, H. H. Kim, J. M. Cannata, G.-S. Chen, and K. K. Shung, in *2007 IEEE International Ultrasonics Symposium Proceedings* (IEEE, 2007), pp. 949–952.
- ³⁰H. J. Lee and S. Zhang, *IEEE Trans. Ultrason. Ferroelectr. Freq. Control* **59**, 1969 (2012).
- ³¹A. Selfridge, G. Kino, and B. Khuri-Yakub, *Appl. Phys. Lett.* **37**, 35 (1980).
- ³²M. Onoe and H. Tiersten, *IEEE Trans. Ultrason. Eng.* **10**, 32–38 (1963).
- ³³Z.-Y. Shen, Y. Xu, and J.-F. Li, *J. Appl. Phys.* **105**, 104103 (2009).
- ³⁴R. Chen, N. E. Cabrera-Munoz, K. H. Lam, H.-S. Hsu, F. Zheng, Q. Zhou, and K. K. Shung, *IEEE Trans. Ultrason. Ferroelectr. Frequency Control* **61**, 1033–1041 (2014).
- ³⁵M. J. Zipparo, K. K. Shung, and T. R. Shrout, *IEEE Trans. Ultrason. Ferroelectr. Freq. Control* **44**, 1038–1048 (1997).
- ³⁶X. Yan, K. H. Lam, X. Li, R. Chen, W. Ren, X. Ren, Q. Zhou, and K. K. Shung, *IEEE Trans. Ultrason. Ferroelectr. Freq. Control* **60**, 1272–1276 (2013).
- ³⁷T. Meeker, *IEEE Trans. Ultrason. Ferroelectr. Freq. Control* **43**, 717–772 (1996).
- ³⁸B. Zhu, N. Y. Chan, J. Dai, K. K. Shung, S. Takeuchi, and Q. Zhou, *IEEE Trans. Ultrason. Ferroelectr. Freq. Control* **60**, 854–857 (2013).
- ³⁹J. Ma, S. Xue, X. Zhao, F. Wang, Y. Tang, Z. Duan, T. Wang, W. Shi, Q. Yue, and H. Zhou, *Appl. Phys. Lett.* **111**, 092903 (2017).
- ⁴⁰J. Ou-Yang, B. Zhu, Y. Zhang, S. Chen, X. Yang, and W. Wei, *Appl. Phys. A* **118**, 1177–1181 (2015).
- ⁴¹Z. Y. Shen, J. F. Li, R. Chen, Q. Zhou, and K. K. Shung, *J. Am. Ceram. Soc.* **94**, 1346–1349 (2011).
- ⁴²P. Sun, Q. Zhou, B. Zhu, D. Wu, C. Hu, J. M. Cannata, J. Tian, P. Han, G. Wang, and K. K. Shung, *IEEE Trans. Ultrason. Ferroelectr. Freq. Control* **56**, 2760–2763 (2009).
- ⁴³Z. Zhang, F. Li, R. Chen, T. Zhang, X. Cao, S. Zhang, T. R. Shrout, H. Zheng, K. K. Shung, and M. S. Humayun, *IEEE Trans. Ultrason. Ferroelectrics Frequency Control* **65**, 223–230 (2018).
- ⁴⁴J. M. Cannata, T. A. Ritter, W.-H. Chen, R. H. Silverman, and K. K. Shung, *IEEE Trans. Ultrason. Ferroelectr. Freq. Control* **50**, 1548–1557 (2003).
- ⁴⁵K. Wang, B. Malić, and J. Wu, *MRS Bull.* **43**, 607–611 (2018).
- ⁴⁶X. Sun, J. Deng, J. Chen, C. Sun, and X. Xing, *J. Am. Ceram. Soc.* **92**, 3033–3036 (2009).
- ⁴⁷V. Y. Topolov, C. R. Bowen, A. N. Isaeva, and A. A. Panich, *Phys. Status Solidi A* **215**, 1700548 (2018).
- ⁴⁸Z. Yang, D. Zeng, H. Wang, C. Zhao, and J. Tan, *Smart Mater. Struct.* **24**, 075029 (2015).
- ⁴⁹Y. Sun, X. Gao, H. Wang, Z. Chen, and Z. Yang, *Appl. Phys. Lett.* **112**, 043903 (2018).